

Quasi-steady emission from repeating fast radio bursts can be explained by magnetar wind nebula

Mukul Bhattacharya^{1,2*}, Kohta Murase^{1,3,4}, Kazumi Kashiyama^{5,6}

¹*Department of Physics; Department of Astronomy & Astrophysics; Center for Multimessenger Astrophysics, Institute for Gravitation and the Cosmos, The Pennsylvania State University, University Park, PA 16802, USA*

²*Department of Physics, Wisconsin IceCube Particle Astrophysics Center, University of Wisconsin, Madison, WI 53703, USA*

³*Center for Gravitational Physics and Quantum Information, Yukawa Institute for Theoretical Physics, Kyoto University, Kyoto, Kyoto 606-8502, Japan*

⁴*School of Natural Sciences, Institute for Advanced Study, Princeton, NJ 08540, USA*

⁵*Astronomical Institute, Graduate School of Science, Tohoku University, Aoba, Sendai 980-8578, Japan*

⁶*Kavli Institute for the Physics and Mathematics of the Universe (Kavli IPMU, WPI), The University of Tokyo, Chiba 277-8582, Japan*

Accepted . Received ; in original form

ABSTRACT

Among over 1000 known fast radio bursts (FRBs), only three sources – FRB 121102 (R1), FRB 190520 (R2) and FRB 201124 (R3) – have been linked to persistent radio sources (PRS). The observed quasi-steady emission is consistent with synchrotron radiation from a composite of magnetar wind nebula (MWN) and supernova (SN) ejecta. We compute the synchrotron flux by solving kinetic equations for energized electrons, considering electromagnetic cascades of electron-positron pairs interacting with nebular photons. For rotation-powered model, a young neutron star (NS) with age $t_{\text{age}} \approx 20$ yr, dipolar magnetic field $B_{\text{dip}} \approx (3 - 5) \times 10^{12}$ G and spin period $P_i \approx 1.5 - 3$ ms in an ultra-stripped SN progenitor can account for emissions from R1 and R2. In contrast, R3 requires $t_{\text{age}} \approx 10$ yr, $B_{\text{dip}} \approx 5.5 \times 10^{13}$ G and $P_i \approx 10$ ms in a conventional core-collapse SN progenitor. For magnetar-flare-powered model, NS aged $t_{\text{age}} \approx 25/40$ yr in a USSN progenitor and $t_{\text{age}} \approx 12.5$ yr in a CCSN progenitor explains the observed flux for R1/R2 and R3, respectively. Finally, we constrain the minimum NS age $t_{\text{age,min}} \sim 1 - 3$ yr from the near-source plasma contribution to observed DM, and $t_{\text{age,min}} \sim 6.5 - 10$ yr based on the absence of radio signal attenuation.

Key words: stars: magnetars, winds, outflows – supernovae: general – transients: fast radio bursts – radiation mechanisms: general

1 INTRODUCTION

Fast radio bursts (FRBs) are energetic millisecond duration pulses of coherent emission, located at cosmological distances, whose physical origin is still debated after a decade since their discovery (Lorimer et al. 2007; Thornton et al. 2013; Spitler et al. 2014; Cordes & Chatterjee 2019). Many theoretical models have been proposed to explain the nature of their progenitors, both for repeating and one-off events (see Platts et al. 2019, for a recent review). The detection of Galactic FRB 200428 and its association with SGR J1935+2154 (Bochenek et al. 2020; CHIME/FRB Collaboration et al. 2020), suggests that FRBs can originate from magnetars born from the core collapse of massive stars (see e.g., Murase et al. 2016; Kumar et al. 2017; Bhattacharya 2019; Kumar & Bošnjak 2020; Lu et al. 2022).

In addition to FRBs, rapidly rotating pulsars and magnetars have been proposed as central engines of super-luminous supernovae (SNe), stripped-envelope SNe and rapidly-rising optical transients (Metzger et al. 2015; Kashiyama et al. 2016; Hotokezaka et al. 2017; Margalit & Metzger 2018). Pulsar wind nebulae (PWNe) are known to be efficient particle accelerators and broadband non-thermal emission has been observed from the nebulae of Galactic PWNe (Tanaka & Takahara 2010, 2013). Murase et al. (2016) proposed quasi-steady synchrotron emission as counterparts of both FRBs and pulsar/magnetar-driven SNe (including SLSNe), suggesting efficient conversion of rotation and/or magnetic energy to particle energies within the nascent MWN of a young NS (e.g., Gaensler & Slane 2006).

Precise localisation of FRBs can provide meaningful insights on their sources, by identifying plausible multi-wavelength counterpart(s) and revealing information about the central engine and its surrounding environment (Michilli

* mbhattachar5@wisc.edu

et al. 2018). However, until date, only three confirmed FRB-PRS associations have been made in the sample of localized FRBs; namely those of FRB 121102 (Chatterjee et al. 2017), FRB 190520 (Niu et al. 2022) and FRB 201124 (Bruni et al. 2023). PRSs are continuum radio sources that are significantly bright ($L_{\text{PRS}} > 10^{29} \text{ erg s}^{-1} \text{ Hz}^{-1}$) and compact ($R_{\text{PRS}} < 1 \text{ pc}$), for them to be related to ongoing star formation in their host galaxy (Nimmo et al. 2022; Dong et al. 2024). The polarisation level is found to be significantly different between the FRB 121102 bursts and its PRS emission (Michilli et al. 2018; Plavin et al. 2022), thereby ruling out the possibility that these emissions are of the same intrinsic nature. Furthermore, there is no clear evidence for either repeaters or non-repeaters to be preferentially associated with PRSs (Law et al. 2022), indicating that these are two separate aspects of the central engine and its environment (Bhandari et al. 2023).

Apart from their actively repeating behaviour and association with a compact PRS, these three FRB sources also exhibit large values of host galaxy dispersion measure ($\text{DM} \sim 150 - 450 \text{ pc cm}^{-3}$) and rotation measure ($\text{RM} \sim 10^3 - 10^5 \text{ rad m}^{-2}$), indicating the presence of a dense magneto-ionic environment near the PRS emission region. This is consistent with synchrotron radiation originating from a compact magnetized nebula surrounding a young NS, embedded behind an expanding SN ejecta shell. If the observed RM primarily arises from the PRS region, the PRS luminosity should be correlated with the large source RM (Yang et al. 2020). Recently, Bruni et al. (2023) confirmed such a correlation with the detection of the third, less luminous PRS associated with FRB 201124 having $\text{RM} \sim 10^3 \text{ rad m}^{-2}$. They suggest that for lower values of RM, the PRS radio luminosity will likely fall below the detection threshold of current radio telescopes.

The PRSs associated with FRB 121102 and FRB 190520 demonstrate a relatively flat spectrum, $S_\nu \propto \nu^\alpha$, for $\sim 1 - 10 \text{ GHz}$ with a spectral index of $\alpha = -0.27 \pm 0.24$ and -0.41 ± 0.04 , respectively (Marcote et al. 2017; Niu et al. 2022). Both these PRSs have a spectral radio luminosity of $(2 - 4) \times 10^{29} \text{ erg s}^{-1} \text{ Hz}^{-1}$ and a flux density $\sim 200 \mu\text{Jy}$ at 3 GHz (Chatterjee et al. 2017; Niu et al. 2022). In contrast, FRB 201124's PRS shows an inverted spectrum from $\nu = 6 - 22 \text{ GHz}$ with $\alpha = 1.00 \pm 0.43$, flux density $\sim 20 \mu\text{Jy}$ at 15 GHz and spectral radio luminosity $5 \times 10^{27} \text{ erg s}^{-1} \text{ Hz}^{-1}$ (Bruni et al. 2023). Long-term variation in the radio flux of PRS can be useful to constrain properties of the source. Rhodes et al. (2023) recently found a $\sim 30\%$ reduction in the flux density of FRB 121102's PRS at 1.3 GHz over a timescale of three years. Similarly, Zhang et al. (2023) reported a $\sim 20\%$ decrease in the flux density of FRB 190520's PRS at 3 GHz from 2020 to 2021.

Energy injection into the magnetized nebula surrounding the central NS can take place due to either the rotational energy of a young NS that spins down over time (Cordes & Wasserman 2016; Connor et al. 2016; Lyutikov et al. 2016; Kashiyama & Murase 2017), or the release of magnetic energy from NS interior due to flares originating close to the magnetar (Lyubarsky 2014; Kulkarni et al. 2014; Kumar et al. 2017; Margalit & Metzger 2018; Zhao & Wang 2021). The injected energy continually drives the expansion of MWN out to the SN ejecta, and the persistent emission is powered by relativistic electrons heated at the termination

shock of the magnetar wind. Efficient conversion of NS rotation/magnetic energy to particle energy in the termination shock region is required to explain the observed quasi-steady radio emission. For rapidly rotating young NS, rotational energy is the primary reservoir which powers the wind nebula as is the case with Galactic PWNe (Tanaka & Takahara 2010). However, for a decades-old magnetar, the interior NS magnetic energy may be more significant in comparison to its rotational energy, as proposed by Margalit & Metzger (2018) to explain the large RM and PRS luminosity of FRB 121102.

The inferred host galaxy DM contribution at $z = 0.241$ for FRB 190520 is $\text{DM}_{\text{host}} \simeq 900 \text{ pc cm}^{-3}$ (Niu et al. 2022), which is a factor of five larger than that of typical FRB host galaxies (James et al. 2022). Zhang et al. (2020) used IllustrisTNG simulations to show that the DM contribution from FRB 190520-like host galaxies at $z \approx 0.2$ is $\text{DM}_{\text{host}} \approx 150 \pm 100 \text{ pc cm}^{-3}$, which indicates a significant near-source DM contribution, possibly due to an expanding young SN remnant (Piro & Gaensler 2018; Zhao & Wang 2021; Katz 2022). Furthermore, FRB 190520's DM decreases with time at the rate $-0.09 \pm 0.02 \text{ pc cm}^{-3} \text{ day}^{-1}$ (Niu et al. 2022), in contrast to the nearly fixed DM of FRB 121102 (Hessels et al. 2019; Oostrum et al. 2020; Li et al. 2021). Such large near-source DM together with its decreasing trend can be explained by an expanding shocked shell of SN remnant (Piro & Gaensler 2018; Katz 2022), whereas the large and decreasing RM (e.g., for FRB 121102, Hilmarsson et al. 2021) arises due to the radiative cooling of electrons injected into the magnetized nebula.

In this work, we propose that FRB sources with an associated PRS are powered by young magnetars embedded in a composite of MWN and SN remnant. The observed quasi-steady emission is generated by synchrotron radiation of the MWN, with the dense SN ejecta contributing a large fraction of the near-source DM. This paper is organised as follows. In Section 2, we discuss the physical model for energy injection from the rotation/magnetar-flare-powered wind region into the magnetized nebula. In Section 3, we describe the combined evolution of the MWN and SN ejecta, which is used to compute synchrotron emission from the magnetized nebula. In Section 4, we present the physical constraints needed to explain the detectable radio emission from the PRSs of all three FRBs. Based on the observed radio spectral energy distribution (SED), light curve and time evolution of the near-source DM for these sources, we constrain the magnetar parameters and that of the SN ejecta in Section 5. We also compare the magnetar parameters derived for the rotation- and magnetar-flare-powered models. We summarize our main results and conclude in Section 6.

2 PHYSICAL MODEL

A highly magnetised pulsar (or magnetar) is likely to remain as a compact remnant once a SN explosion takes place. The rotational and/or magnetic energy extracted by the outgoing relativistic wind is injected into the associated nebula which then powers the synchrotron emission from the SN ejecta, detectable at radio frequencies. Figure 1 shows a schematic diagram of a rapidly rotating young magnetar surrounded by a magnetized nebula and SN ejecta. The spin-

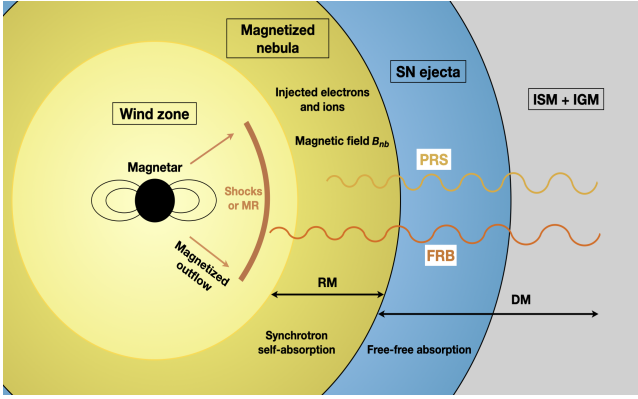


Figure 1. Schematic picture of a magnetar surrounded by magnetized wind nebula and baryonic SN ejecta. Magnetar flares and/or rotationally powered outflows inject particles and magnetic energy into the nebula. Synchrotron radiation, observed as PRS associated with the FRB, is emitted by energetic electrons gyrating within the magnetized nebula. The radio emission is observable once the system becomes optically thin to various processes.

down/magnetic energy powers outflows that are accelerated in the wind zone between the NS light cylinder and the nebula. The energized electrons once injected into the nebula gyrate along the magnetic fields to drive the persistent radio emission that is associated with the FRB. The resultant non-thermal emission is powered by synchrotron radiation in the magnetized nebula and SN ejecta. While most of the RM originates from the magnetic fields in the nebula, bulk of the near-source DM is accumulated in the SN ejecta. FRB persistent emission is observable once the system becomes optically thin to synchrotron self-absorption in the nebula and free-free absorption in the ejecta.

2.1 Energy source of quasi-steady emission

Murase et al. (2016) considered a young pulsar/magnetar-driven SN as the source of synchrotron emission from wind nebula. Here we extend their model to explain the persistent radio emission from three sources namely FRBs 121102, 190520 and 201124. We first discuss the energy injection mechanism for these sources, considering both rotation- and magnetic-powered scenarios.

The rotation-powered model has been studied extensively in the context of Crab Nebula (e.g., Connor et al. 2016; Cordes & Wasserman 2016; Lyutikov et al. 2016). The intrinsic energy arising from NS rotation is $\mathcal{E}_{\text{rot},i} = 0.175 M_{\text{ns}} R_{\text{ns}}^2 (2\pi/P_i)^2 \approx (1.9 \times 10^{52} \text{ erg}) P_{i,-3}^{-2}$, where $M_{\text{ns}} = 1.4 M_{\odot}$ is the NS mass, $R_{\text{ns}} = 12 \text{ km}$ is the NS radius and P_i is its initial spin period. Rotation energy is extracted by unipolar induction with spindown luminosity

$$L_{\text{sd}} \approx (7.2 \times 10^{45} \text{ erg/s}) B_{\text{dip},13}^2 P_{i,-3}^{-4} \left(1 + \frac{t}{t_{\text{sd}}}\right)^{-2}, \quad (1)$$

where B_{dip} is the dipolar magnetic field and $t_{\text{sd}} \approx (0.12 \text{ yr}) B_{\text{dip},13}^{-2} P_{i,-3}^2$ is the characteristic spindown timescale.

Magnetar powered models are promising as evidenced by the recent detection of FRB 200428 from a Galactic magnetar (Bochenek et al. 2020; CHIME/FRB Collaboration et al. 2020). The magnetic energy $\mathcal{E}_{\text{B,int}} \approx$

$B_{\text{int}}^2 R_{\text{ns}}^3 / 6 = (3 \times 10^{49} \text{ erg}) B_{\text{int},16}^2$ for a given interior magnetic field B_{int} , is expected to be more significant in comparison to the rotation energy for a NS with age $t_{\text{age}} \gtrsim \text{few} \times 10 \text{ yr}$. Comparing the minimum energy, $\mathcal{E}_{\text{FRB,min}} \approx f_b \mathcal{F}_{\text{FRB}} \mathcal{R}_{\text{FRB}} t_{\text{age}}$, needed to explain a repeating FRB with magnetic energy $\mathcal{E}_{\text{B,int}}$ provides a lower limit $B_{\text{int}} \gtrsim (10^{15} \text{ G}) f_b^{1/2} \mathcal{F}_{\text{FRB},40}^{1/2} \mathcal{R}_{\text{FRB},-3}^{1/2} t_{\text{age},9.5}^{1/2}$ (see Kashiyama & Murase 2017). Here f_b is the beaming factor, \mathcal{F}_{FRB} is the FRB fluence, \mathcal{R}_{FRB} is the repetition rate for FRB and t_{age} is the NS age.

Magnetic energy injection has been proposed to explain the PRS associated with FRB 121102 along with its high rotation measure. Margalit & Metzger (2018) considered a power-law energy injection rate given by

$$L_{\text{mag}} = (\alpha - 1) \frac{\mathcal{E}_{\text{B,int}}}{t_{\text{inj}}} \left(\frac{t}{t_{\text{inj}}}\right)^{-\alpha}, \quad (2)$$

where $t_{\text{inj}} \approx 0.6 \text{ yr}$ is the time when the onset of energy injection occurs and $\alpha \approx 1.3$ is the power-law index. Here t_{inj} is determined by the timescale for magnetic flux to start leaking out of the magnetar core. Beloborodov (2017) proposed that t_{inj} from flares can be comparable to the pair freeze-out timescale $t_{\pm} \sim 0.1 \text{ yr}$. Although the energy injection index α can depend on the nature of the FRB source, Margalit & Metzger (2018) showed that $\alpha \gtrsim 1$ adequately explains the radio SED of the PRS associated with FRB 121102. This implies that the rate of FRB activity slows down over time or the flares become less energetic on average. Although L_{mag} here is modeled with a smooth function of time, the energy release from magnetars can also occur intermittently. For time $t < t_{\text{inj}}$, energy injection is dominated by rotation and the total injected energy is $\mathcal{E}_{\text{tot}}(t < t_{\text{inj}}) = \int_0^t L_{\text{sd}}(t) dt$. In contrast, the interior magnetic energy leaks out into the nebula for $t \geq t_{\text{inj}}$, and therefore $\mathcal{E}_{\text{tot}}(t \geq t_{\text{inj}}) = \int_0^t [L_{\text{sd}}(t) + L_{\text{mag}}(t)] dt$.

2.2 Properties of injected particles

2.2.1 Energy injection

Both rotational energy injection (Dai et al. 2017; Kashiyama & Murase 2017) and magnetic energy injection (Beloborodov 2017; Margalit & Metzger 2018; Zhao & Wang 2021) models have been proposed to explain the PRS luminosity as well as the large RM detected for FRB 121102 (Michilli et al. 2018). The observed persistent radio emission from FRBs can be interpreted as synchrotron emission from electrons in the nebula.

The upper limit of the energy stored in the nebula is

$$\begin{aligned} \text{Max}(\mathcal{E}_e^{\text{inj}}) &\approx \epsilon_e \mathcal{N}_{\text{sd}}(t_{\text{age}}) \int_0^{t_{\text{age}}} L_{\text{sd}}(t') dt' \\ &+ \epsilon_e \mathcal{N}_{\text{mag}}(t_{\text{age}}) \int_0^{t_{\text{age}}} L_{\text{mag}}(t') dt'. \end{aligned} \quad (3)$$

Here $\epsilon_e \approx 1 - \epsilon_B$ is the injection efficiency, $\mathcal{N}_{\text{sd/mag}}(t_{\text{age}}) = 1$ for $t_{\text{age}} < t_{\text{sd/mag}}$ and $\mathcal{N}_{\text{sd/mag}}(t_{\text{age}}) = (t_{\text{sd/mag}}/t_{\text{age}})[1 + \log(t_{\text{age}}/t_{\text{sd/mag}})]$ for $t_{\text{age}} > t_{\text{sd/mag}}$, accounts for the effect of adiabatic energy loss from the magnetar wind nebula which is especially significant at late times. As radiative energy losses are also relevant, equation (3) provides a strict upper limit for energy contained in the nebula.

2.2.2 Particle number distribution

The rotational or magnetic energy is injected into the nebula together with the particles. The injected particles are accelerated to relativistic energies inside or around the termination shock before entering the nebula. The lepton injection rate \dot{n}_e^{inj} is given by a broken power-law function (see e.g., Tanaka & Takahara 2010; Murase et al. 2015)

$$\mathcal{E}_e^2 \dot{n}_e^{\text{inj}} = \frac{3\epsilon_e(L_{\text{sd}} + L_{\text{mag}})}{4\pi R_{\text{nb}}^2 c \mathcal{R}_0} \begin{cases} (\gamma_e/\gamma_b)^{2-q_1}, & \gamma_e \leq \gamma_b \\ (\gamma_e/\gamma_b)^{2-q_2}, & \gamma_b < \gamma_e \end{cases} \quad (4)$$

where R_{nb} is the nebula radius, $\mathcal{R}_0 \sim (2 - q_1)^{-1} + (q_2 - 2)^{-1} \sim 5$ is the correction factor for the lepton normalization, $q_1 < 2$ and $q_2 \geq 2$ are the low- and high-energy spectral indices. For our analysis, we adopt the characteristic LF of the accelerated leptons to be $\gamma_b \sim 10^5$ for rotation-powered and $\gamma_b \sim 10^3$ for magnetic-powered models. The spectral indices are $q_1 = 1.5$ and $q_2 = 2.5$ for rotation-powered scenario, and $q_1 = q_2 = 2.0$ for magnetic-powered case. We assume $10^3 \leq \gamma_e \leq 10^7$, based on the multi-wavelength modelling of young Galactic PWNe (Tanaka & Takahara 2013). The effective pair multiplicity can be generally expressed in terms of γ_b , q_1 and q_2 (see Murase et al. 2015).

3 PROPERTIES OF THE COMPACT PRS

Due to energy injection into the young magnetar, the wind nebula and SN ejecta tend to evolve together. Here we discuss their combined evolution and compute the synchrotron emission from the magnetised nebula that leads to the observed persistent radio counterparts for FRB sources.

3.1 MWN and SNR evolution

The density profile of the SN ejecta can be described using a power-law function $\rho_{\text{ej}} = (3 - \delta)M_{\text{ej}}/4\pi R_{\text{ej}}^3 (R/R_{\text{ej}})^{-\delta}$ (Chevalier & Soker 1989; Kasen & Bildsten 2010), where $\delta = 1$ is the fiducial value of the index, M_{ej} is the ejecta mass and R_{ej} is the ejecta radius. The time evolution of the SN ejecta internal energy is given by

$$\frac{d\mathcal{E}_{\text{int}}}{dt} = \epsilon_e f_{\text{dep, sd/mag}} L_{\text{sd/mag}} + f_{\text{dep, rd}} L_{\text{rd}} - L_{\text{sn}} - \frac{\mathcal{E}_{\text{int}}}{R_{\text{ej}}} \frac{dR_{\text{ej}}}{dt} \quad (5)$$

where $f_{\text{dep, sd/mag/rd}}$ is the energy fraction deposited from NS spindown/magnetic field injection/radioactive decay estimated from Kashiyama et al. (2016), L_{rd} is the radioactive decay power, L_{sn} is the SN luminosity and the last term represents energy loss due to adiabatic expansion.

3.2 Synchrotron emission

We estimate the radii of the ejecta and nebula using (see also, Metzger et al. 2014; Kashiyama et al. 2016)

$$\frac{dR_{\text{nb}}}{dt} = \sqrt{\frac{7}{6(3-\delta)} \frac{\mathcal{E}_{\text{tot}}}{M_{\text{ej}}} \left(\frac{R_{\text{nb}}}{R_{\text{ej}}}\right)^{3-\delta}} + \frac{R_{\text{nb}}}{t}, \quad (6)$$

$$\frac{dR_{\text{ej}}}{dt} = V_{\text{ej}}, \quad (7)$$

where the first term on the right-hand side of equation (6) corresponds to the nebula velocity in the

ejecta rest frame and V_{ej} is the ejecta velocity. The initial ejecta velocity is almost constant, $V_{\text{ej},i} \approx 10^4 \text{ km/s} (\mathcal{E}_{\text{sn}}/10^{51} \text{ erg})^{1/2} (M_{\text{ej}}/M_{\odot})^{-1/2}$, in the Sedov-Taylor expansion phase prior to energy injection. If $R_{\text{nb}} > R_{\text{ej}}$, the ejecta and nebula radii evolve together with the same velocity $dR_{\text{ej}}/dt = dR_{\text{nb}}/dt = V_{\text{ej},f} = \sqrt{2(\mathcal{E}_{\text{tot}} + \mathcal{E}_{\text{SN}})/M_{\text{ej}}}$ as the injected energy significantly accelerates the ejecta through the magnetised wind.

The average magnetic field in the nebula is given by $B_{\text{nb}} = \sqrt{6\mathcal{E}_B/R_{\text{nb}}^3}$, where \mathcal{E}_B is the magnetic energy in the nebula. The magnetic energy in the nebula evolves as (see e.g., Murase et al. 2016, 2021)

$$\frac{d\mathcal{E}_B}{dt} = \epsilon_B(L_{\text{sd}} + L_{\text{mag}}) - c_B \frac{\mathcal{E}_B}{R_{\text{nb}}} \frac{dR_{\text{nb}}}{dt}, \quad (8)$$

In this work, we consider $c_B = 0$ in the limit when energy loss due to adiabatic expansion is negligible, as done previously for Galactic PWNe (Tanaka & Takahara 2010) and pulsar-powered PWNe (Murase et al. 2015, 2016).

We compute the synchrotron emission from the nebula by solving kinetic equations for the photons and electrons (see e.g., Murase et al. 2021)

$$\begin{aligned} \frac{\partial n_{\mathcal{E}_\gamma}}{\partial t} &= -n_{\mathcal{E}_\gamma} \left(\frac{1}{t_{\text{comp}}^{\text{nb}}} + \frac{1}{t_{\text{esc}}^{\text{nb}}} + \frac{1}{t_{\gamma\gamma}} \right) + \frac{\partial}{\partial t} (n_{\mathcal{E}_\gamma}^{\text{IC}} + n_{\mathcal{E}_\gamma}^{\text{syn}}), \\ \frac{\partial n_{\mathcal{E}_e}}{\partial t} &= -\frac{\partial}{\partial \mathcal{E}_e} [(P_{\text{ad}} + P_{\text{syn}} + P_{\text{IC}})n_{\mathcal{E}_e}] + \frac{\partial n_{\mathcal{E}_e}^{\gamma\gamma}}{\partial t} + \dot{n}_{\mathcal{E}_e}^{\text{inj}} \end{aligned} \quad (9)$$

where $t_{\text{comp}}^{\text{nb}}$ is the Comptonisation timescale in the nebula, $t_{\text{esc}}^{\text{nb}} = R_{\text{nb}}/c$ is the photon escape timescale, $t_{\gamma\gamma}$ is the photon annihilation timescale, $\partial n_{\mathcal{E}_\gamma}^{\text{IC/syn}}/\partial t$ is the photon generation rate from IC/synchrotron process. P_{ad} , P_{syn} and P_{IC} are the energy-loss rates due to adiabatic expansion, synchrotron radiation and IC, respectively, $\partial n_{\mathcal{E}_e}^{\gamma\gamma}/\partial t$ is the electron production rate from photon annihilation and $\dot{n}_{\mathcal{E}_e}^{\text{inj}}$ is the electron injection rate from equation (4).

4 PHYSICAL CONDITIONS

Here we examine the physical conditions that are imposed on the parameters of the magnetised nebula and SN ejecta which we derived earlier. These conditions are necessary to qualitatively explain the observations for the persistent radio counterparts associated with FRBs.

4.1 Constraints on model parameters

We list here the constraints on the model parameters: the dipolar magnetic field B_{dip} , the initial spin period P_i , NS age t_{age} , SN ejecta mass M_{ej} and explosion energy \mathcal{E}_{SN} .

- *Magnetised nebula energy requirement:* The minimum energy in relativistic electrons required to explain the quasi-steady radio emission from FRB sources should be less than the maximum energy stored in the nebula which is given by $\text{Max}(\mathcal{E}_e^{\text{inj}})$ (see e.g., equation 3). The observed quasi-steady radio spectrum for FRBs can be fitted by

$$\nu F_\nu \approx \frac{\mathcal{L}_{\text{nb}}}{4\pi d_L^2} \begin{cases} (\nu/\bar{\nu})^{p_1}, & \nu < \bar{\nu} \\ (\nu/\bar{\nu})^{p_2}, & \nu \geq \bar{\nu} \end{cases} \quad (10)$$

Here $\bar{\nu} \sim 10 - 30 \text{ GHz}$, $\mathcal{L}_{\text{nb}} \sim 10^{38} - 10^{39} \text{ erg/s}$, $p_1 \sim 0.6 - 2.0$

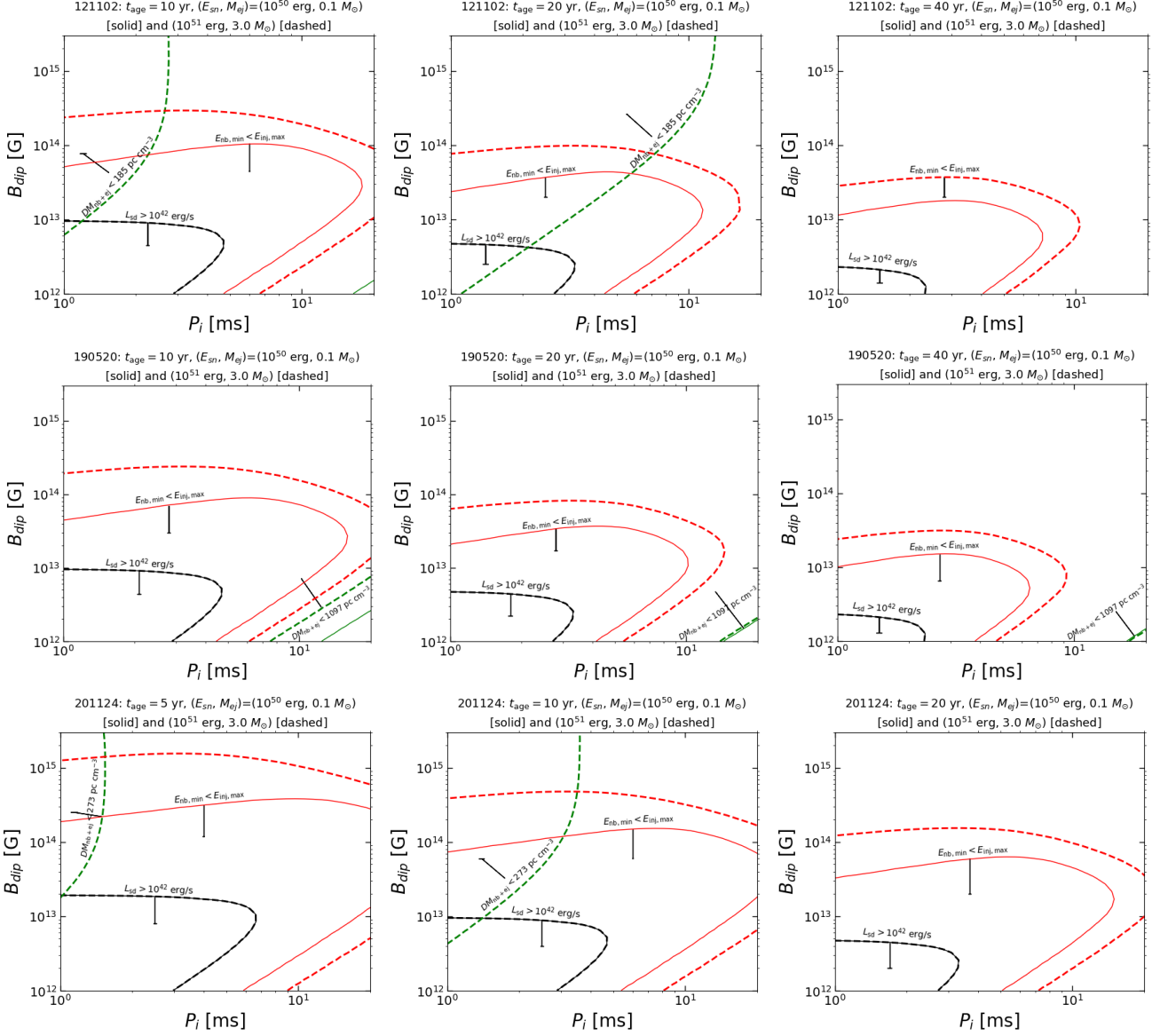


Figure 2. Constraints on NS parameters B_{dip} and P_i from the nebula energy requirement (red curves), ejecta and nebula contribution to the source DM (green curves), and the NS spindown luminosity (black curves) are shown for FRB 121102 in top row, FRB 190520 in middle row and FRB 201124 in bottom row. In each panel, the solid curves show the results for $(E_{\text{sn}}, M_{\text{ej}}) = (10^{50} \text{ erg}, 0.1 M_{\odot})$ while the dashed curves show results for $(E_{\text{sn}}, M_{\text{ej}}) = (10^{51} \text{ erg}, 3.0 M_{\odot})$. For the magnetic energy injection, we fix $B_{\text{int}} = 10^{16} \text{ G}$ and $t_{\text{inj}} = 0.6 \text{ yr}$ for all cases. For FRBs 121102 and 190520, we vary $t_{\text{age}} = 10 \text{ yr}$ (left panel), 20 yr (middle panel) and 40 yr (right panel) as $t_{\text{obs}} > 5 \text{ yr}$. In case of FRB 201124, results are shown for $t_{\text{age}} = 5 \text{ yr}$ (left panel), 10 yr (middle panel) and 20 yr (right panel).

and $p_2 \sim -0.5$ for the three FRBs currently detected with a confirmed PRS (Chatterjee et al. 2017; Niu et al. 2022; Bruni et al. 2023). The luminosity distance $d_L \sim 400 - 1200 \text{ Mpc}$ is determined by the known redshift $z \sim 0.1 - 0.2$.

We assume that the bolometric luminosity for nebula \mathcal{L}_{nb} peaks in the radio bands, to estimate the minimum required energy $\text{Min}(\mathcal{E}_e^{\text{nb}})$ stored in the electrons. The LF for radio-emitting electron is $\gamma_e \approx (4\pi m_e c \bar{v} / 3e B_{\text{nb}})^{1/2}$ and the energy loss rate is $P_e \approx (4/3)\sigma_T c \gamma_e^2 B_{\text{nb}}^2 / 8\pi$. The total number of electrons in the magnetised nebula is roughly $N_e \approx \mathcal{L}_{\text{nb}} / P_e$ and the minimum required energy in the nebula is then (see

Kashiyama & Murase 2017)

$$\text{Min}(\mathcal{E}_e^{\text{nb}}) = N_e \gamma_e m_e c^2 \approx \frac{3\sqrt{3}(\pi e m_e c)^{1/2} \mathcal{L}_{\text{nb}}}{\sigma_T \bar{v}^{1/2} B_{\text{nb}}^{3/2}} \quad (11)$$

Therefore, the rotational and magnetic energy injection should be large enough to provide sufficient energy to the nebula. Also, the NS should be young enough such that adiabatic energy losses are not significant.

- *Constraint on source DM:* The number density of free electrons in the SN ejecta and magnetised nebula are given by $n_{e,\text{ej}} \approx 3M_{\text{ej}} / (4\pi R_{\text{ej}}^3 \mu_e \bar{A} m_{\text{H}})$ and $n_{e,\text{nb}} \approx 3M_{\text{nb}} / (4\pi R_{\text{nb}}^3 \mu_e \bar{A} m_{\text{H}})$, respectively. Here $M_{\text{ej}/\text{nb}}$ is the

ejecta/nebula mass, $\bar{A} = 10$ is the mean atomic mass number and $\mu_e \approx 1$ for the singly ionized state corresponding to electron temperature $\mathcal{T}_e \sim 10^4$ K (see [Kashiyama & Murase 2017](#)). The total DM contribution close to the source, from the SN ejecta and magnetised wind nebula is

$$DM_{\text{ns}} \approx DM_{\text{ej}} + DM_{\text{nb}} \approx n_{e,\text{ej}} R_{\text{ej}} + n_{e,\text{nb}} R_{\text{nb}}, \quad (12)$$

where R_{nb} and R_{ej} are obtained by solving equations (6) and (7). Although M_{nb} is uncertain, a reasonable lower limit can be obtained using the Goldreich-Julian (GJ) density ([Goldreich & Julian 1969](#))

$$M_{\text{nb}}/t_{\text{age}} \gtrsim \dot{M}_{\text{GJ}} \approx (2.4 \times 10^{-11} M_{\odot}/\text{s}) \mu_{\pm,6} B_{\text{int},15} P_{i,-3}^{-2}, \quad (13)$$

where $\mu_{\pm} \sim 10^{5-6}$ is the pair multiplicity defined as the ratio of the pair density to the Goldreich-Julian (GJ) density. The ejecta DM contribution from the SNR should evolve over time as $DM_{\text{ej}} \propto t^{-2}$. The NS needs to be old enough such that $DM_{\text{ns}} \approx n_{e,\text{ej}} R_{\text{ej}} + n_{e,\text{nb}} R_{\text{nb}} \lesssim DM_{\text{host}}$.

- *Non-attenuation of radio signal:* Radio pulses that are produced in the NS magnetosphere can be diminished either through scattering or absorption process in the SN ejecta and magnetised nebula. Free-free absorption in the SN ejecta is one of the relevant processes and the NS should be old enough such that the opacity at \sim GHz frequencies (see e.g., [Murase et al. 2017](#))

$$\tau_{\text{ff}} \approx 2.1 \times 10^{-25} \mathcal{T}_{e,4}^{-1.35} \int dr n_{e,\text{ej}} n_{i,\text{ej}} \bar{Z}^2, \quad (14)$$

does not exceed unity. Here $\bar{Z} \sim \bar{A}/2$ and $n_{i,\text{ej}}$ is the number density of ions in the ejecta. Furthermore, it is expected that synchrotron self-absorption (SSA) is subdominant in magnetised nebula indicating that ([Yang et al. 2016](#))

$$\tau_{\text{sa}} = R_{\text{nb}} \int \mathcal{E}_e \frac{dn_{\mathcal{E}_e}}{d\mathcal{E}_e} \sigma_{\text{sa}}(\nu, \mathcal{E}_e) \quad (15)$$

is also less than unity, for a energy-dependent SSA cross section σ_{sa} ([Ghisellini & Svensson 1991](#)).

- *Size constraint for FRB source:* Lastly, the size of the magnetised nebula should not exceed the observed upper limit on the size of the PRS, given by its angular size and luminosity distance for the FRB. From VLBI and VLA observations of FRBs 121102, 190520 and 201124, $R_{\text{nb}} \lesssim 1 - 10$ pc (see [Tendulkar et al. 2017](#); [Niu et al. 2022](#); [Bruni et al. 2023](#)).

4.2 Implications for FRBs detected with PRS

To compute the synchrotron emission from magnetized nebula, we first need to constrain the NS parameters including $B_{\text{dip}} \sim 10^{12} - 10^{15}$ G, $P_i \sim 1 - 30$ ms and $t_{\text{age}} \gtrsim t_{\text{obs}}$, where t_{obs} is the time since initial detection of the FRB source. For our analysis, we consider two progenitors: (a) an ultra-stripped SNe with $M_{\text{ej}} \sim 0.1 M_{\odot}$ and $\mathcal{E}_{\text{SN}} \sim 10^{50}$ erg (USSN model), and (b) a conventional core-collapse SNe with $M_{\text{ej}} \sim 3.0 M_{\odot}$ and $\mathcal{E}_{\text{SN}} \sim 10^{51}$ erg (CCSN model). For the injected magnetic energy (see equation 2), we adopt $B_{\text{int}} = 10^{16}$ G and $t_{\text{inj}} = 0.6$ yr as in [Margalit & Metzger \(2018\)](#). We discuss the combination of NS parameters B_{dip} , P_i and t_{age} for which the magnetar satisfies all the necessary constraints as discussed in Section 4.1.

Figure 2 shows the constraints on $P_i - B_{\text{dip}}$ parameter space for the nebula energy requirement in red, DM contribution from the ejecta and nebula in green, and the NS spindown luminosity in black. The results for FRB 121102 (R1), FRB 190520 (R2) and FRB 201124 (R3) are shown in the top, middle and bottom row panels, respectively, with solid/dashed curves corresponding to the USSN/CCSN model in each panel. Along with the NS spindown luminosity, we also consider magnetic energy injection with $B_{\text{int}} = 10^{16}$ G and $t_{\text{inj}} = 0.6$ yr for all cases. We find that the DM criteria for SN ejecta and MWN contribution ($DM_{\text{ej+nb}} < DM_{\text{host}}$), and the MWN minimum energy requirement ($\varepsilon_{\text{nb,min}} < \varepsilon_{\text{inj,max}}$) are the most constraining. In the left, center and right column panels, we vary the NS age: $t_{\text{age}} \sim 10 - 40$ yr for R1 and R2, and $t_{\text{age}} \sim 5 - 20$ yr for R3. With an increase in t_{age} , $DM_{\text{nb+ej}}$ decreases faster due to expansion as compared to the reduction in $\varepsilon_{\text{inj,max}}$ from adiabatic energy losses, thereby allowing a larger $P_i - B_{\text{dip}}$ parameter space. For a given P_i , $DM_{\text{ej+nb}}$ reduces faster for a larger B_{dip} , as more energy gets injected into the SN ejecta within a shorter timescale leading to a faster ejecta expansion. However, a smaller B_{dip} is allowed for a given P_i to prevent considerable adiabatic losses.

For a given t_{age} , it is easier to satisfy the DM criterion ($DM_{\text{ej+nb}} < DM_{\text{host}}$) in the order R2 > R1 > R3, which directly follows from the inferred DM_{host} values for these three localized FRBs. However, the energy criterion ($\varepsilon_{\text{nb,min}} < \varepsilon_{\text{inj,max}}$) is satisfied in a larger $P_i - B_{\text{dip}}$ parameter space for R3 as compared to the other two sources, primarily due to smaller q_1 leading to more energy injection near the peak of the spectrum (see equation 10). Although the qualitative trends in parameter constraints obtained from the near-source DM and nebula energy criteria are effectively same, for both USSN and CCSN progenitors at a given t_{age} , the DM (energy) constraint is harder (easier) to satisfy for the CCSN case due to their larger M_{ej} (\mathcal{E}_{SN}). For $t_{\text{age}} \gtrsim 10$ yr and USSN (CCSN) progenitor, the allowed parameter space satisfying both these conditions is limited to: $P_i \sim 1 - 10$ ms and $B_{\text{dip}} \sim 10^{12} - 10^{14}$ G ($P_i \sim 1 - 2.5$ ms and $B_{\text{dip}} \sim 5 \times 10^{12} - 2 \times 10^{14}$ G) for R1, $P_i \sim 1 - 10$ ms and $B_{\text{dip}} \sim 10^{12} - 10^{14}$ G ($P_i \sim 1 - 20$ ms and $B_{\text{dip}} \sim 10^{12} - 2 \times 10^{14}$ G) for R2, and $P_i \sim 1 - 20$ ms and $B_{\text{dip}} \sim 10^{12} - 10^{14}$ G ($P_i \sim 1 - 3$ ms and $B_{\text{dip}} \sim 5 \times 10^{12} - 3 \times 10^{14}$ G) for R3. For both USSN and CCSN cases, the parameter space satisfying $L_{\text{sd}} \gtrsim 10^{42}$ erg/s generally overlaps with that allowed by $DM_{\text{ej+nb}} < DM_{\text{host}}$ and $\varepsilon_{\text{nb,min}} < \varepsilon_{\text{inj,max}}$ criteria, especially for $t_{\text{age}} \gtrsim 10$ yr. This indicates that the NS spindown luminosity is likely to be the primary energy source for these three FRBs.

5 OBSERVED FRB PROPERTIES

With the constraints obtained for NS parameters (P_i , B_{dip} , t_{age}) in Section 4, we compute the spectral energy distribution (SED) and light curve of the associated PRS, in addition to the time evolution of source DM for the three FRBs to compare them with the radio data. Efficient conversion of rotational energy to particle energy in the termination shock region is required to explain the observed quasi-steady radio emission. We consider two scenarios: (a) rotation-powered model with ($\epsilon_B = 0.01$, $\gamma_b = 10^5$, $q_1 = 1.5$, $q_2 = 2.5$), and

(b) magnetar-flare-powered model with ($\epsilon_B = 0.1$, $\gamma_b = 10^3$, $q_1 = q_2 = 2$). We use a opacity $\kappa = 0.05 \text{ cm}^2/\text{g}$ for the SN ejecta, and set the NS mass $M_{\text{NS}} = 1.4 M_{\odot}$, radius $R_{\text{NS}} = 10 \text{ km}$ and initial SN explosion radius $R_0 = 10^6 \text{ km}$.

5.1 SED & light curve of the PRS

We first numerically compute the radio SEDs for the nebular emission using the code developed by [Murase et al. \(2015\)](#), which takes into account the effect of electron-positron pairs relevant for emission at $t \gtrsim t_{\text{sd}}$. We incorporate the inverse Compton and synchrotron emission processes to solve the time-dependent kinetic equation (9), and account for electromagnetic cascades. The external radiation fields are taken to be cosmic microwave background (CMB) and extragalactic background light (EBL). In our calculations, we have included the effect of synchrotron self-absorption (SSA) in magnetised nebula and free-free absorption in the SN ejecta, along with the Razin effect.

For the rotation-powered model and both progenitor types, the effect of t_{age} on the radio spectral energy distribution (SED) is shown for R1/R2/R3 in the left/center/right panels of Figure 3, with the corresponding radio data shown with filled circles. As expected, the synchrotron flux is suppressed for larger NS age ($t_{\text{age}} \gg t_{\text{sd}}$) due to considerable adiabatic energy losses at late times. Based on comparison with the observed radio flux, we find a best-fit $t_{\text{age}} \approx 20$ (20) [8] yr for USSN and $t_{\text{age}} \approx 32$ (25) [10] yr for CCSN models, corresponding to R1 (R2) [R3]. The low-energy synchrotron flux is highly suppressed due to SSA, especially for the large M_{ej} in case of CCSN progenitors. While the USSN model seems marginally more promising for both R1 and R2 to explain the observed PRS emission at smaller energies ($\nu \sim 1 \text{ GHz}$), only CCSN model satisfactorily explains the observed emission for R3 due to the large suppression of radio flux at smaller energies.

Next we use the best-fit t_{age} obtained from Figure 3 for each FRB to study the effect of NS parameters on the synchrotron radio flux. In particular, we analyze the effect of dipolar magnetic field B_{dip} on the radio SED as shown in the top-row panels of Figure 4. As in Figure 3, the results for R1/R2/R3 are shown in the left/center/right column panels, with the same representation for progenitor types and radio data shown as filled circles. We find that dipolar field $B_{\text{dip}} = 3 \times 10^{12}$ (5×10^{12}) [5.5×10^{13}] G explains the observed radio flux for R1 (R2) [R3]. With further increase in B_{dip} , the NS spindown timescale ($t_{\text{sd}} \propto B_{\text{dip}}^{-2} P_i^2$) becomes smaller for a given P_i , which results in energy injection into the nebula at early times. This is then accompanied by significant adiabatic losses which leads to a reduced flux.

The effect of NS spin period P_i on the radio SED is shown in the bottom-row panels of Figure 4. As expected, the observed radio flux tends to be larger for a smaller P_i as more rotational energy can be extracted from the NS. However, this difference is less noticeable for larger B_{dip} (like in case of R3), as $t_{\text{age}} \gg t_{\text{sd}}$ results in significant adiabatic energy loss. We find that $P_i = 3$ (1.5) [10] ms best explains the observed radio flux for R1 (R2) [R3]. The low-energy radio flux is suppressed for both fixed P_i and fixed B_{dip} cases for the CCSN model, especially for R3, due to stronger SSA attenuation in the nebula. In summary, we find that a NS with $t_{\text{age}} \approx 20 \text{ yr}$, $B_{\text{dip}} \approx (3-5) \times 10^{12} \text{ G}$ and $P_i \approx 1.5-3 \text{ ms}$

in a USSN progenitor can explain the observed PRS flux for R1 and R2. However, in case of R3, the source is more likely to be a younger NS with $t_{\text{age}} \approx 10 \text{ yr}$, $B_{\text{dip}} \approx 5.5 \times 10^{13} \text{ G}$ and $P_i \approx 10 \text{ ms}$ in a CCSN progenitor. The properties of the central NS and its surrounding ejecta material are consistent with those deduced from previous studies (see e.g., [Margalit & Metzger 2018](#); [Zhao & Wang 2021](#)).

We next compute the radio light curves associated with synchrotron emission from the magnetized nebula. To study the effect of progenitor model (USSN/CCSN), we use the best-fit B_{dip} and P_i values obtained for each FRB source from Figure 4. The light curve data at various frequencies is obtained from: [Marcote et al. \(2017\)](#); [Plavin et al. \(2022\)](#); [Rhodes et al. \(2023\)](#) for R1, [Niu et al. \(2022\)](#); [Zhang et al. \(2023\)](#) for R2, and [Bruni et al. \(2023\)](#) for R3. The corresponding NS age is set to $t_{\text{age}} = 20$ (20) [10] yr from Figure 3. We find that the radio flux predictions from the USSN and CCSN models, for the best-fit NS parameters, are effectively indistinguishable based on current observations for both R1 and R2. However, in case of R3, recent observations at $\nu = 6 \text{ GHz}$ clearly favor the CCSN progenitor model, which also agrees with our results based on the radio SEDs shown in Figure 4. As expected, the radio light curve peaks at a later time and with a smaller synchrotron peak for larger ejecta mass M_{ej} and/or larger SN explosion energy \mathcal{E}_{sn} for the CCSN model. Although the synchrotron flux can reduce with an increase in M_{ej} , especially for smaller $t_{\text{age}} \sim 10 \text{ yr}$ as in the case of R3, the spectrum is generally softer due to a smaller synchrotron peak. Lastly, the variation in synchrotron peak flux is marginally higher for CCSN progenitors with a larger SN explosion energy \mathcal{E}_{sn} .

5.2 NS age constraint from DM evolution

For a FRB source located at redshift z , the observed DM can be separated into four primary components,

$$\text{DM}_{\text{obs}} = \text{DM}_{\text{MW}} + \text{DM}_{\text{halo}} + \text{DM}_{\text{IGM}} + \frac{\text{DM}_{\text{host}} + \text{DM}_{\text{ns}}}{(1+z)} \quad (16)$$

where $\text{DM}_{\text{MW}/\text{halo}}$ is the contribution from the Milky Way interstellar medium (ISM)/halo, DM_{IGM} is the contribution from the intergalactic medium (IGM) and DM_{host} is the contribution from the FRB host galaxy including its halo. Here DM_{ns} only includes contributions from the MWN and SN ejecta that are near source. While the long-term DM variation is due to the expanding SNR ([Yang & Zhang 2017](#); [Piro & Gaensler 2018](#)), random fluctuations in the DM can be caused by turbulent motions of filament ([Katz 2021](#)).

From theoretical and data-driven estimates of $\text{DM}_{\text{MW}/\text{halo}}$ and DM_{IGM} , assuming models for the average electron number density in these media (see e.g., [Cordes & Lazio 2002, 2003](#); [Planck Collaboration et al. 2016](#); [Prochaska & Zheng 2019](#); [Platts et al. 2020](#)), the inferred $\text{DM}_{\text{host}} + \text{DM}_{\text{ns}}$ in equation (16) indicates significant contributions from the host galaxy disk, circumgalactic medium and near-source medium for most FRBs that have an associated PRS (see e.g., [Law et al. 2022](#)). In fact, from previous studies ([Chatterjee et al. 2017](#); [Niu et al. 2022](#); [Bruni et al. 2023](#); [Lee et al. 2023](#)), we know that the host galaxy and near-source contribution $\text{DM}_{\text{host}} + \text{DM}_{\text{ns}} \sim 140$ (430) [185] pc cm^{-3} for R1 (R2) [R3]

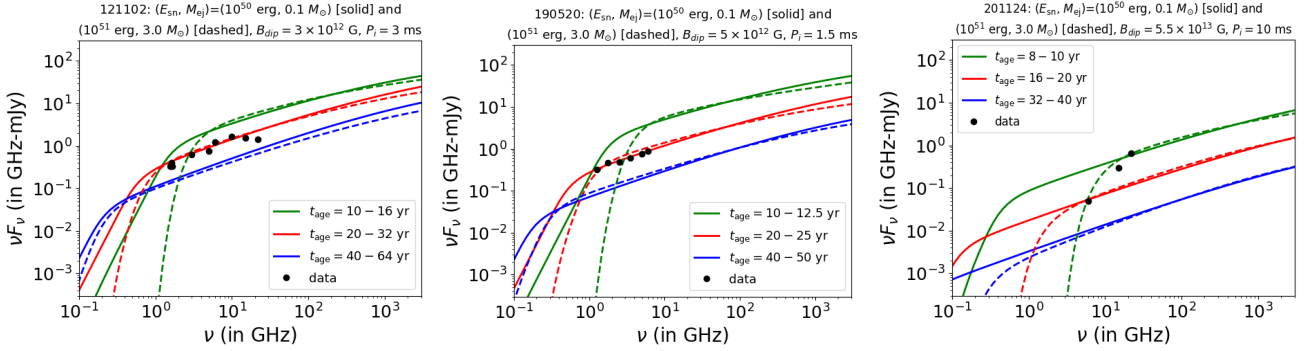


Figure 3. Effect of NS age (t_{age}) on the spectral energy distribution of persistent radio emission is shown for FRB 121102 (190520) [201124] in the left (center) [right] panel. Data from radio observations of each PRS source is shown with filled circles. In each panel, we show the results for USSN/CCSN progenitors using solid/dashed curves, for a fixed (B_{dip}, P_i) combination and varying t_{age} – including the best-fit NS age for the respective source. We assume the rotation-powered model with $\epsilon_B = 0.01$, $\gamma_b = 10^5$, $q_1 = 1.5$ and $q_2 = 2.5$.

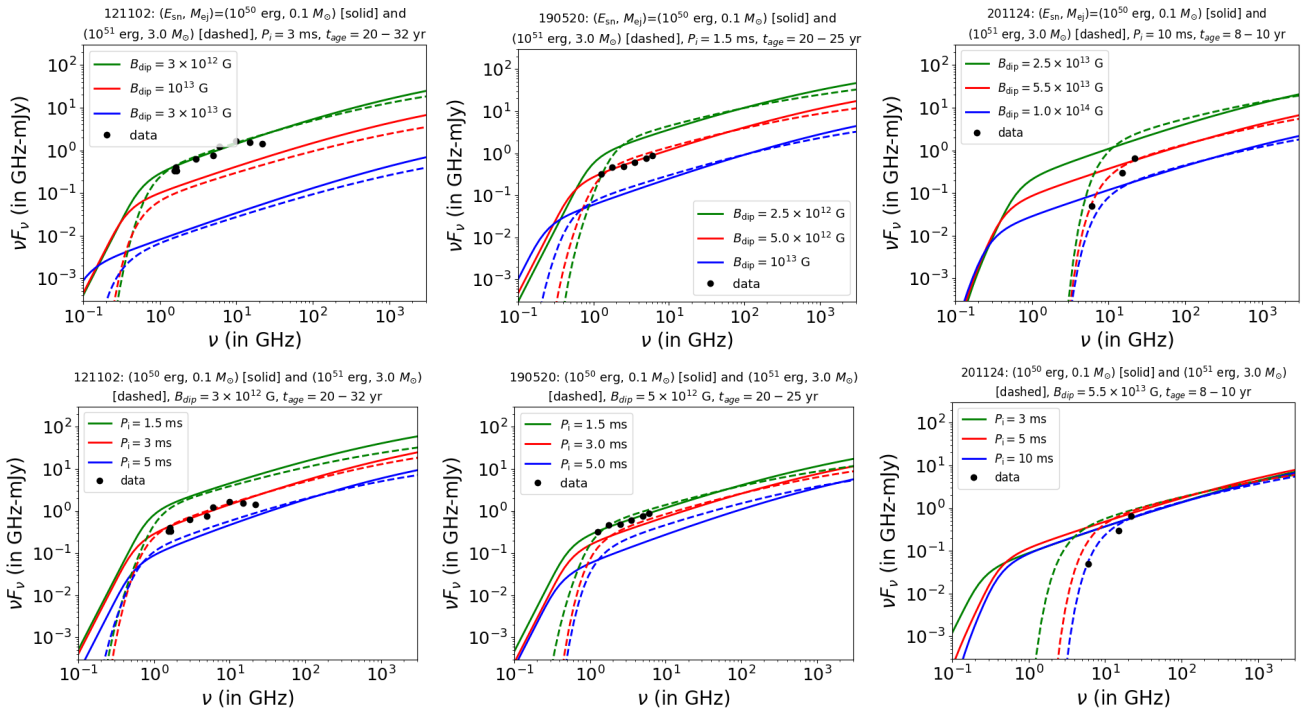


Figure 4. The effect of NS dipolar magnetic field B_{dip} (in top row) and initial spin period P_i (in bottom row) on the spectral energy distribution of persistent radio emission is shown for FRB 121102 (190520) [201124] in the left (center) [right] column panels. In each panel, the data from radio observations is shown with filled circles and results for USSN/CCSN progenitors are shown using solid/dashed curves. For each FRB, we fix t_{age} to the best-fit value obtained from Figure 3 and vary B_{dip} or P_i – including their best-fit combinations for the respective source. As in Figure 3, we assume microphysical parameters corresponding to the rotation-powered model.

can be considerable. Using Illustris simulations to model the electron number density along various lines of sight, Zhang et al. (2020) showed that the typical DM contribution from host galaxies at $z \sim 0.2$, that are similar to the three FRBs considered here, can be $\sim 50 - 250 \text{ pc cm}^{-3}$.

For a young NS, the magnetised nebula and SN ejecta can be dense enough to provide a large DM which is inconsistent with the observations. DM contribution from the near-source medium should decrease with NS age as the MWN and SN ejecta expand over time. In contrast to the nearly unchangeable DM of FRB 121102 (Hessels et al. 2019; Oostrum et al. 2020; Li et al. 2021), the DM of FRB 190520 decreases

with the rate of $\sim 0.1 \text{ pc cm}^{-3}$ per day (Niu et al. 2022). We use detailed calculations of ionization and radiation transport for young rapidly rotating NS to predict contributions from the MWN and SN ejecta to FRB DM (see Kashiyama & Murase 2017; Margalit & Metzger 2018).

Figure 6 shows the time evolution of the inferred FRB host galaxy and near source DM contribution, $\text{DM}_{\text{host}} + \text{DM}_{\text{ns}}$, for R1 (R2) [R3] in the left (center) [right] panel. To analyze the DM contributions from the MWN and expanding SN ejecta, for a given progenitor model i.e. USSN/CCSN, we fix the NS parameters to their best-fit values as in Figure 5. The host galaxy DM contribution (in-

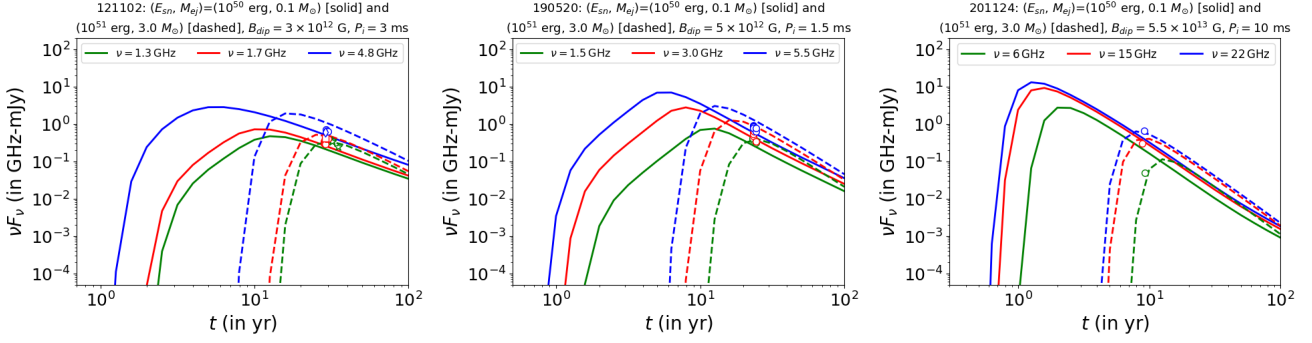


Figure 5. Light curves for the persistent radio emission associated with FRB 121102 (190520) [201124] are shown in the left (center) [right] panel. The corresponding data at various radio frequencies for each source is shown using unfilled circles. As earlier, the results for USSN and CCSN progenitors are shown with solid and dashed curves, respectively. We fix the NS parameters B_{dip} , P_i and t_{age} to their best-fit values obtained from Figures 3 and 4 for the rotation-powered model.

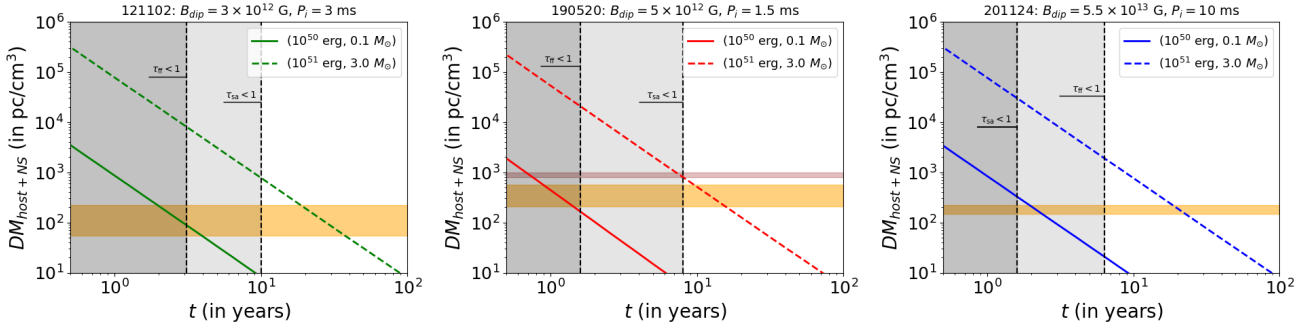


Figure 6. Time evolution of $DM_{\text{host}+\text{ns}}$ is shown for FRB 121102 (190520) [201124] in the left (center) [right] panel, by considering contribution from the expanding SN ejecta and MWN. Results for USSN and CCSN models are shown with solid and dashed curves, respectively, and the best-fit NS parameters (B_{dip} , P_i) are the same as those in Figure 5. The shaded yellow region in each panel denotes the host galaxy DM contribution including its uncertainty. For FRB 190520, we also show the previously estimated $DM_{\text{host}+\text{ns}}$, which likely includes contribution from foreground galaxy groups and clusters (Lee et al. 2023). The dashed vertical lines (for the CCSN cases) correspond to minimum t_{age} obtained by imposing $\tau_{\text{sa}} < 1$ in the MWN and $\tau_{\text{ff}} < 1$ in the SN ejecta, respectively, with the grey shaded areas signifying the regions that are disallowed by the detectability of PRS.

Table 1. The best fit NS parameters (dipolar magnetic field B_{dip} , initial spin period P_i , age t_{age}) are listed for the rotation-powered model with microphysical parameters $\epsilon_B = 0.01$, $\gamma_b = 10^5$, $q_1 = 1.5$ and $q_2 = 2.5$. The results are tabulated for both USSN ($E_{\text{sn}} = 10^{50}$ erg, $M_{\text{ej}} = 0.1 M_{\odot}$) and CCSN ($E_{\text{sn}} = 10^{51}$ erg, $M_{\text{ej}} = 3.0 M_{\odot}$) progenitors for the respective FRB PRSs.

| Source | Progenitor | $(E_{\text{sn}}, M_{\text{ej}})$ | t_{age} | B_{dip} | P_i |
|------------|------------|--|------------------|--------------------------------|--------|
| FRB 121102 | USSN | $(10^{50} \text{ erg}, 0.1 M_{\odot})$ | 20 yr | $3 \times 10^{12} \text{ G}$ | 3.0 ms |
| | CCSN | $(10^{51} \text{ erg}, 3.0 M_{\odot})$ | 32 yr | $3 \times 10^{12} \text{ G}$ | 3.0 ms |
| FRB 190520 | USSN | $(10^{50} \text{ erg}, 0.1 M_{\odot})$ | 20 yr | $5 \times 10^{12} \text{ G}$ | 1.5 ms |
| | CCSN | $(10^{51} \text{ erg}, 3.0 M_{\odot})$ | 25 yr | $5 \times 10^{12} \text{ G}$ | 1.5 ms |
| FRB 201124 | USSN | $(10^{50} \text{ erg}, 0.1 M_{\odot})$ | 8 yr | $5.5 \times 10^{13} \text{ G}$ | 10 ms |
| | CCSN | $(10^{51} \text{ erg}, 3.0 M_{\odot})$ | 10 yr | $5.5 \times 10^{13} \text{ G}$ | 10 ms |

cluding its relative uncertainty) is shown in each panel with the shaded yellow region; the shaded magenta region for R2 denotes the possibly overestimated DM_{host} due to significant contributions from the foreground galaxies and clusters (see e.g. Lee et al. 2023). As expected, the DM contribution from the SN ejecta and magnetized nebula is substantially higher for CCSN progenitor models as they have a larger M_{ej} . The

contribution from the magnetised nebula to DM_{ns} is almost negligible compared to that from the denser SN ejecta.

A lower limit on the source age t_{age} follows from the requirement that the SN ejecta should not be significantly dense to overproduce DM relative to DM_{obs} . We find the minimum NS age allowed by the near-source DM constraint to be $t_{\text{age,min}} \sim 1 - 3$ yr. The dashed vertical lines and the associated grey-shaded regions in Figure 6 correspond to

the condition that the SN ejecta and the magnetized nebula should allow for the propagation of radio waves outside the source environment, and therefore be transparent to free-free absorption ($\tau_{\text{ff}} \lesssim 1$) and synchrotron self-absorption ($\tau_{\text{sa}} \lesssim 1$), respectively. This condition imposes a somewhat stronger constraint on the minimum NS age with $t_{\text{age, min}} \sim 10$ yr for R1, ~ 8 yr for R2 and ~ 6.5 yr for R3. Our inferred best-fit t_{age} from Figure 3 exceeds this minimum NS age required by the absorption criterion.

5.3 Rotation and magnetic powered models

Energy injected by the rotating magnetar drives the MWN and SN ejecta to evolve together, and the observed quasi-steady emission is powered by the synchrotron radiation generated from the magnetized nebula. For young rapidly rotating NS, the rotational energy is the primary energy reservoir that powers the magnetised nebula and it has been studied in detail for Galactic PWNe (Tanaka & Takahara 2010, 2013). For a typical NS with mass $M_{\text{ns}} = 1.4 M_{\odot}$ and radius $R_{\text{ns}} = 12$ km, the rotational energy is given by $\mathcal{E}_{\text{rot, i}} \approx (1.9 \times 10^{52} \text{ erg}) P_{i, -3}^{-2}$. However, for a magnetar of age $t_{\text{age}} \gg t_{\text{sd}} \approx (0.12 \text{ yr}) B_{\text{dip, 13}}^{-2} P_{i, -3}^2$, the central NS may spin down considerably over time such that its interior magnetic energy, $\mathcal{E}_{\text{B, int}} \approx B_{\text{int}}^2 R_{\text{ns}}^3 / 6 = (3 \times 10^{49} \text{ erg}) B_{\text{int, 16}}^2$, is comparable or even larger than $\mathcal{E}_{\text{rot, i}}$.

In our analysis, we incorporate models for rotational energy injection proposed by Kashiyama & Murase (2017) and energy injection due to magnetar flares based on Margalit & Metzger (2018), to compute the total energy injected into the magnetar wind nebula (see equation 3). However, the microphysical parameters ϵ_B , γ_b , q_1 and q_2 that determine the actual energy injection rate into the radiating electrons are given by equation (4). In the previous sections, we considered a rotation-powered model with $\epsilon_B = 0.01$, $\gamma_b = 10^5$, $q_1 = 1.5$ and $q_2 = 2.5$. The corresponding best-fit NS parameters (t_{age} , B_{dip} , P_i) are listed in Table 1 for USSN and CCSN progenitor models, based on the radio SEDs obtained for all three sources in Figures 3 and 4.

We now consider the scenario where the energy injection from magnetar flares exceeds that from NS rotation i.e. $\mathcal{E}_{\text{B, int}} \gtrsim \mathcal{E}_{\text{rot, i}}$, with $P_i = 300$ ms, $B_{\text{int}} = 5 \times 10^{16}$ G and $B_{\text{dip}} \sim 5 \times 10^{14} - 5 \times 10^{15}$ G. We study the effect of varying t_{age} on the radio SED of synchrotron emission for the magnetar-flare-powered model with $\epsilon_B = 0.1$, $\gamma_b = 10^3$ and $q_1 = q_2 = 2.0$. The results for R1/R2/R3 are shown in the left/center/right panel of Figure 7, with solid/dashed curves denoting USSN/CCSN progenitors and filled circles corresponding to the radio data for each source. As for the rotation-powered model in Figure 3, the late-time ($t_{\text{age}} \gg t_{\text{sd}}$) and low-energy ($\nu \lesssim 1$ GHz) synchrotron flux is suppressed due to significant adiabatic losses and SSA, respectively. However, the high-energy radio flux typically attains smaller values compared to the rotation-powered model to then gradually fall off. This is expected as the energy injection into particles occurs at smaller $\gamma_b \sim 5 \times 10^3$ for the magnetar-flare-powered model. We find that the USSN progenitor model better explains the low-energy ($\nu \lesssim 1$ GHz) radio SED for both R1 and R2, corresponding to best-fit $t_{\text{age}} \approx 25$ yr and ≈ 40 yr, respectively. On the contrary, the radio SED for R3 is only explained by the CCSN model

with a best-fit $t_{\text{age}} \approx 12.5$ yr while accounting for the large suppression in radio flux at smaller energies.

For the magnetar-flare-powered model, we show the radio light curves for the persistent emission associated with each FRB source in Figure 8. We use the best-fit B_{dip} and P_i values obtained from radio SED fits in Figure 7 for each FRB source, with the corresponding NS age set to $t_{\text{age}} = 25$ (40) [12.5] yr. In contrast to the results obtained in Figure 5 for the rotation-powered model, we find that the flux predictions from the USSN model are favored by the radio data, especially at smaller frequencies, for both R1 and R2. In case of R3, the radio observations at smaller frequency $\nu \approx 6$ GHz favor the CCSN model over the USSN progenitor model. These results are consistent with those obtained from the radio SED fits for the magnetar-flare-powered model ($\epsilon_B = 0.1$, $\gamma_b = 10^3$, $q_1 = q_2 = 2.0$) in Figure 7. The best-fit NS parameters (t_{age} , B_{dip}) for the magnetar-flare-powered scenario with $P_i \approx 300$ ms are listed in Table 2, for both USSN and CCSN models, based on the radio SED and light curve results shown in Figure 7 and 8, respectively.

6 SUMMARY & DISCUSSIONS

Magnetars and rapidly rotating pulsars and magnetars have been studied extensively as central engines of SLSNe and FRBs, as they can naturally explain the quasi-steady synchrotron emission from their nascent pulsar/magnetar wind nebulae. These central engines can provide a unified picture of SLSNe, stripped-envelope SNe, FRBs as well as long GRBs. Non-thermal nebular emission has been observed for many Galactic PWNe, which suggests that a significant fraction of the wind magnetic energy can be utilized for accelerating particles. Murase et al. (2016) proposed quasi-steady synchrotron emission as a potential probe of FRB progenitors and also explored their possible connection to pulsar/magnetar-driven SNe including SLSNe.

Till date, three repeating FRBs namely FRB 121102, FRB 190520 and FRB 201124 have been localized and associated with compact persistent radio sources (Chatterjee et al. 2017; Niu et al. 2022; Bruni et al. 2023). In this study, we consider the scenario whereby quasi-steady emission from such FRB sources are powered by young rapidly rotating magnetars that are embedded in a composite of magnetized wind nebula and SN ejecta. We have presented a detailed theoretical model here to numerically compute the radio SEDs for nebular emission by solving the time-dependent kinetic equations for photons and electrons in the MWN. To test the SNe progenitor models, we considered two cases: (a) an ultra-stripped SNe with $M_{\text{ej}} = 0.1 M_{\odot}$ and $E_{\text{sn}} = 10^{50}$ erg, and (b) a conventional core-collapse SNe with $M_{\text{ej}} = 3.0 M_{\odot}$ and $E_{\text{sn}} = 10^{51}$ erg.

While rotational energy from a young NS is likely to be the primary reservoir that powers magnetized nebula, energy released from the dissipation of interior magnetic fields can be significant at later times $t_{\text{age}} \gg t_{\text{sd}}$ once the NS spins down. We estimated the total energy injected into the MWN based on the NS rotational energy injection model proposed by Kashiyama & Murase (2017). For the magnetar flare energy injection model, we adopted $B_{\text{int}} = 10^{16}$ G and $t_{\text{inj}} = 0.6$ yr as suggested by Margalit & Metzger (2018).

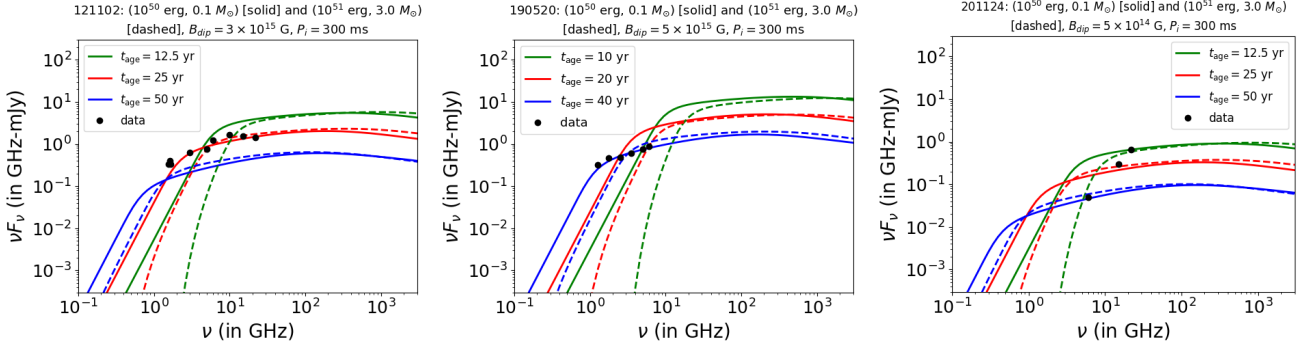


Figure 7. Effect of NS age (t_{age}) on the radio SED of persistent emission from FRB 121102 (190520) [201124] source is shown in the left (center) [right] panel. The fluxes for synchrotron emission are shown for magnetar-flare-powered energy injection model with $\epsilon_B = 0.1$, $\gamma_b = 10^3$, $q_1 = q_2 = 2.0$. For each source, we fix $P_i = 300$ ms and $B_{\text{dip}} \sim (0.01 - 0.1) B_{\text{int}} \approx 5 \times 10^{14} - 5 \times 10^{15}$ G to vary the NS age within a range that includes the best-fit t_{age} . In each panel, the SED data from radio observations is shown with filled circles and the results for USSN/CCSN progenitors are shown using solid/dashed curves.

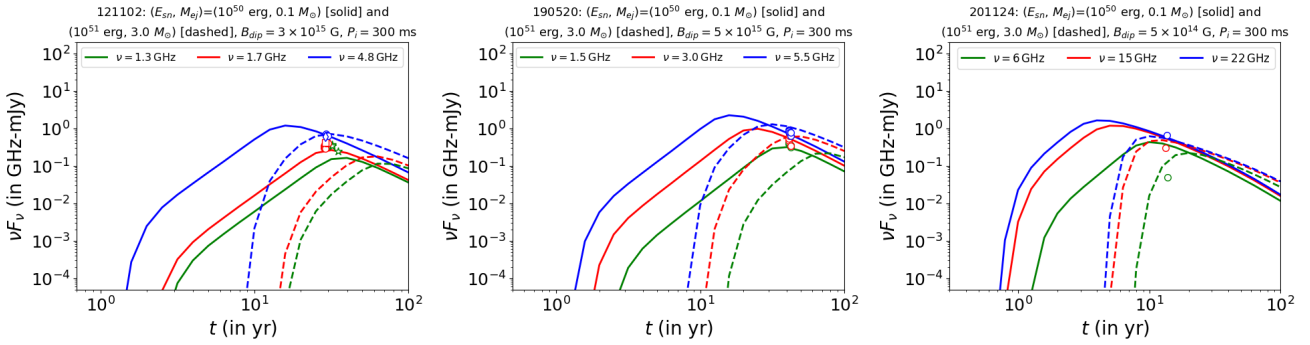


Figure 8. Radio light curves for persistent emission associated with FRB 121102 (190520) [201124] are shown in the left (center) [right] panel. Corresponding data at various frequencies is shown using unfilled circles for each source. The solid and dashed curves here denote the results for USSN and CCSN progenitors, respectively. We fix the NS parameters (B_{dip} , P_i , t_{age}) to their best-fit values as obtained from Figure 7 for the magnetar-flare-powered model.

Table 2. Same as Table 1, but for magnetar-flare-powered model with microphysical parameters $\epsilon_B = 0.1$, $\gamma_b = 10^3$, $q_1 = q_2 = 2.0$. We set $P_i = 300$ ms for all cases listed here. The corresponding radio SED results for all three sources considered are shown in Figure 7.

| Source | Progenitor | $(E_{\text{sn}}, M_{\text{ej}})$ | t_{age} | B_{dip} |
|------------|------------|--|------------------|----------------------|
| FRB 121102 | USSN | $(10^{50} \text{ erg}, 0.1 M_{\odot})$ | 25 yr | 3×10^{15} G |
| | CCSN | $(10^{51} \text{ erg}, 3.0 M_{\odot})$ | 25 yr | 3×10^{15} G |
| FRB 190520 | USSN | $(10^{50} \text{ erg}, 0.1 M_{\odot})$ | 40 yr | 5×10^{15} G |
| | CCSN | $(10^{51} \text{ erg}, 3.0 M_{\odot})$ | 40 yr | 5×10^{15} G |
| FRB 201124 | USSN | $(10^{50} \text{ erg}, 0.1 M_{\odot})$ | 12.5 yr | 5×10^{14} G |
| | CCSN | $(10^{51} \text{ erg}, 3.0 M_{\odot})$ | 12.5 yr | 5×10^{14} G |

In addition to the SNe progenitor and energy injection models, synchrotron flux from the magnetized nebula is determined by NS parameters such as $B_{\text{dip}} \sim 10^{12} - 10^{15}$ G, $P_i \sim 1 - 30$ ms and $t_{\text{age}} \gtrsim t_{\text{obs}}$.

We first estimated the allowed combinations of these parameters using physical constraints from: (a) energy injected into the magnetized nebula ($\epsilon_{\text{nb,min}} < \epsilon_{\text{inj,max}}$), (b) near-source DM contribution from the SN ejecta and MWN ($\text{DM}_{\text{ej+nb}} < \text{DM}_{\text{host}}$), (c) non-attenuation of radio signal due to free-free absorption and synchrotron self-absorption

($\tau_{\text{ff}}, \tau_{\text{sa}} \lesssim 1$), and (d) size of the magnetized nebula ($R_{\text{nb}} \lesssim 10$ pc). The corresponding results for B_{dip} , P_i and t_{age} are shown in Figure 2. We showed that $\epsilon_{\text{nb,min}} < \epsilon_{\text{inj,max}}$ and $\text{DM}_{\text{ej+nb}} < \text{DM}_{\text{host}}$ are the most constraining for the range of parameters and models we considered. For $t_{\text{age}} \gtrsim 10$ yr and USSN progenitor, the allowed (P_i , B_{dip}) parameter space is: (1–10 ms, 10^{12-14} G) for R1 and R2, and (1–20 ms, 10^{12-14} G) for R3. The corresponding parameter space for a CCSN progenitor is: (1–2.5 ms, $5 \times 10^{12} - 2 \times 10^{14}$ G) for R1, (1–20 ms, $10^{12} - 2 \times 10^{14}$ G) for R2, and (1–3 ms,

$5 \times 10^{12} - 3 \times 10^{14}$ G) for R3. For both progenitor types and $t_{\text{age}} \gtrsim 10$ yr, we found that the parameter space satisfying $L_{\text{sd}} > 10^{42}$ erg/s overlaps with the allowed (P_i , B_{dip}) parameter space, which indicates that the NS rotational energy is likely to be the primary energy reservoir for these FRB sources detected with persistent radio counterparts. As the flux decline rate is expected to be proportional to the current NS spindown timescale, t_{age} can also be inferred from detailed follow-up observations of the PRS.

The localisation of R1 and R2 in a dwarf host galaxy with high specific star-formation rate (Chatterjee et al. 2017; Tendulkar et al. 2017) suggested a connection between FRBs and SLSN progenitors (Perley et al. 2016), as also previously pointed out by Murase et al. (2016). Modeling the quasi-steady nebular emission is therefore important to constrain the FRB source properties as the radio emission can be significantly absorbed in the MWN and SN ejecta at early times $t_{\text{age}} \lesssim$ few yrs. SSA in the magnetized nebula and free-free absorption in the SN ejecta are the primary processes that can suppress the low-energy synchrotron flux for SNe progenitors with large ejecta mass and/or explosion energy. To this end, we compute the radio SEDs and light curves for synchrotron emission from the magnetized nebula using the code developed by Murase et al. (2015). We included the inverse Compton and synchrotron emission processes to solve the kinetic equations (see equation 9) to account for electromagnetic cascades in electron-positron pairs with the photons available from the magnetized nebula.

We first considered the rotation-powered model with microscopic parameters $\epsilon_B = 1 - \epsilon_e = 0.01$, $\gamma_b = 10^5$, $q_1 = 1.5$ and $q_2 = 2.5$. We found that the observed radio flux for both R1 and R2 are consistent with an NS of $t_{\text{age}} \approx 20$ yr in a USSN progenitor. However, the observed persistent emission for R3 can only be explained with the CCSN model for a young NS aged $t_{\text{age}} \approx 10$ yr. Although the synchrotron flux at lower energies is highly suppressed due to SSA, this effect is most prominent for R3 even at energies $\nu \lesssim 5$ GHz and therefore suggests a larger M_{ej} (see Figure 3). Contrarily, the larger radio flux at $\nu \approx 1$ GHz along with a harder energy spectra for R1 and R2 is better explained by the USSN progenitor with a smaller M_{ej} . An increase in B_{dip} may not necessarily lead to a brighter radio emission as the NS spindown timescale $t_{\text{sd}} \propto B_{\text{dip}}^{-2} P_i^2$ becomes smaller, thereby resulting in more energy loss due to adiabatic expansion even at early times. From our radio SED estimates, we inferred that the observed PRS flux for R1 and R2 can be explained by an NS with magnetic field $B_{\text{dip}} = (3-5) \times 10^{12}$ G and initial spin period $P_i = 1.5-3$ ms, whereas $B_{\text{dip}} = 5.5 \times 10^{13}$ G and $P_i = 10$ ms in case of R3 as shown in Figure 4.

We also tested the alternate scenario whereby energy injection into the nebula is dominated by magnetar flares, corresponding to microscopic parameters $\epsilon_B = 1 - \epsilon_e = 0.1$, $\gamma_b = 10^3$ and $q_1 = q_2 = 2$. For this case, we fixed the NS parameters to $P_i = 300$ ms, $B_{\text{int}} = 5 \times 10^{16}$ G and $B_{\text{dip}} = 5 \times 10^{14-15}$ G and deduced the typical t_{age} such that the MWN can power the persistent radio emission. For R1 and R2, we found that the USSN progenitor model best explains the low-energy radio SED for $t_{\text{age}} \approx 25$ yr and ≈ 40 yr, respectively. Large suppression in the observed radio flux for R3 implied that the source is likely to be a young

NS with $t_{\text{age}} \approx 12.5$ yr located within a CCSN progenitor with larger ejecta mass as shown in Figure 7.

The observed flux density of a PRS can also exhibit variability across long timescales that are likely to be intrinsic to the source. In a recent study, Rhodes et al. (2023) reported a $\sim 30\%$ reduction in the flux density of R1's PRS at 1.3 GHz over three years (from 2019 to 2022) with the MeerKAT telescope. Similarly, Zhang et al. (2023) reported a $\sim 20\%$ reduction in the radio flux of R2's PRS from their 3 GHz Very Large Array (VLA) observations in 2020 and 2021. Such long-term variation in the PRS radio flux can be instrumental in constraining the properties of the near-source region. Based on the predictions for radio light curves and their comparison with the current data in Figure 5, we found that the USSN and CCSN progenitor models are effectively indistinguishable for both R1 and R2. However, recent observations (Bruni et al. 2023) for R3's PRS favor the CCSN model, in agreement with our radio SED results from Figures 3 and 4.

While the persistent radio emission arises from the relativistic plasma, the DM contribution comes primarily from the cold plasma. If large luminosities for PRSs could be correlated with large DM_{host} for these sources, that would have tremendous diagnostic power. The inferred $\text{DM}_{\text{host}} + \text{DM}_{\text{ns}}$ for these three FRBs indicates substantial contribution from the near-source plasma and circumgalactic medium. Using ionization and radiation transport models for the young NS, we estimated the contributions from the magnetized nebula and the SN ejecta to show that the latter dominates for typical NS parameters. In Figure 6, we obtained a minimum NS age $t_{\text{age, min}} \sim 1 - 3$ yr for the three FRB sources considered such that the SN ejecta is not significantly dense to overproduce observed DM. Non-attenuation of radio signal due to free-free absorption in the ejecta and synchrotron self-absorption in the nebula provides a stronger constraint with $t_{\text{age, min}} \approx 10$ (8) [6.5] yr for R1 (R2) [R3]. It should be noted that the inferred near-source DM is subject to some uncertainty as the pair multiplicity in our models can be uncertain (see Murase et al. 2015, for a detailed discussion).

Our optimal parameter values for B_{dip} , P_i , t_{age} , M_{ej} and E_{sn} are consistent with those derived from previous studies (see e.g., Kashiyama et al. 2016; Yang & Dai 2019; Zhao & Wang 2021). For a pair-dominated wind, Yang & Dai (2019) proposed that persistent radio counterparts to FRBs could arise from MWN powered by a magnetar without surrounding SN ejecta. However, their model could not explain the time evolution of source DM and free-free absorption in the SN ejecta. Recently, Chen & Tong (2024) used a one-zone PWN model to explain the observed quasi-steady emission from R1 and R2. Both these works, however, assumed a constant energy injection rate into a freely expanding nebula. In contrast, Margalit & Metzger (2018) and Zhao & Wang (2021) modelled the energy injection into MWN using a more realistic time-dependent function similar to our work. The predicted $t_{\text{age}} \sim 10 - 40$ yr and $E_{\text{sn}} \sim 10^{50} - 10^{51}$ erg for FRB 121102 from Margalit & Metzger (2018) agrees well with our estimates. Similarly, Zhao & Wang (2021) derived $B_{\text{dip}} \approx 0.1 B_{\text{int}} \sim (2-4) \times 10^{15}$ G and $t_{\text{age}} \sim 14 - 22$ yr from the radio SEDs of R1 and R2. In both these works, the dominant energy injection channel into the nebula was intermittent magnetar flares and a constant nebula/ejecta velocity was assumed. In our analysis, we improved upon these works

by first deriving constraints on the NS and ejecta parameters using observed properties (DM, energy, PRS size, radio signal non-attenuation), to then self-consistently compute the synchrotron flux generated by energized electrons considering both NS rotational and magnetic energy injection scenarios, for nebula/ejecta velocity that is driven by the time-dependent energy injection rate into the magnetized nebula.

If repeating FRBs were to arise from host galaxies that preferentially harbor SLSNe, their rates would be smaller $\sim 0.01\%$ of CCSNe (Quimby et al. 2013). Conversely, if these sources were associated with either ultra-stripped SNe or AICs, their rates should be somewhat higher $\sim 0.1 - 1\%$ of CCSNe (Ruiter et al. 2009; Tauris et al. 2013). Once the number density of repeating FRBs is well constrained from observations, it would facilitate the distinction between these possibilities. Future searches for radio counterparts of pulsar-driven SN candidates, including SLSNe, should give us crucial information on their relationship with FRBs. This is especially true for luminous transients with rapid rotation $P_i \sim 1 - 30$ ms, that are powered by the spin-down luminosity of the NS rather than its magnetic energy. Such nebular emission would be non-thermal, and therefore, easily distinguishable from Galactic thermal sources.

Recently, Xing et al. (2024) reported the detection of a GeV gamma-ray flare lasting ~ 15 sec associated with the hyper-active repeating FRB 20240114A. Our MWN model naturally predicts the existence of such energetic gamma-ray flares in the forward shock region which can result from magnetic energy dissipation within the nebula (see also Murase et al. 2016). Furthermore, hard X-ray emission can also serve as another promising signal for the parameters that account for both SLSNe and FRBs (Metzger & Piro 2014; Kashiyama et al. 2016). A fraction of X-rays can be absorbed by SN ejecta to be re-emitted as thermal emission leading to an optical/UV transient on timescales of days. However, the optical depth of pairs in the nebula can suppress the thermalization efficiency of L_{sd} . For the cases where nebular X-rays are sufficiently energetic to reionize the ejecta, non-thermal X-rays can escape the ejecta unattenuated with a peak luminosity and timescale that is similar to optical radiation.

ACKNOWLEDGEMENTS

We thank Ke Fang and Pawan Kumar for useful discussions and comments. M.B. acknowledges support from the Eberly Research Fellowship at the Pennsylvania State University and the Simons Collaboration on Extreme Electrodynamics of Compact Sources (SCEECS) Postdoctoral Fellowship at the Wisconsin IceCube Particle Astrophysics Center (WIPAC), University of Wisconsin-Madison. The work of K.M. is supported by the NSF Grant No. AST-2108466, No. AST-2108467, and AST-2308021, and KAKENHI No. 20H05852.

DATA AVAILABILITY

The data underlying this article will be shared on reasonable request to the corresponding author.

REFERENCES

- Beloborodov A. M., 2017, *ApJL*, 843, L26
 Bhandari S., et al., 2023, *ApJL*, 958, L19
 Bhattacharya M., 2019, *arXiv e-prints*, p. arXiv:1907.11992
 Bochenek C. D., Ravi V., Belov K. V., Hallinan G., Kocz J., Kulkarni S. R., McKenna D. L., 2020, *Nature*, 587, 59
 Bruni G., et al., 2023, *arXiv e-prints*, p. arXiv:2312.15296
 CHIME/FRB Collaboration et al., 2020, *Nature*, 587, 54
 Chatterjee S., et al., 2017, *Nature*, 541, 58
 Chen Y., Tong H., 2024, *arXiv e-prints*, p. arXiv:2405.07446
 Chevalier R. A., Soker N., 1989, *ApJ*, 341, 867
 Connor L., Sievers J., Pen U.-L., 2016, *MNRAS*, 458, L19
 Cordes J. M., Chatterjee S., 2019, *ARA&A*, 57, 417
 Cordes J. M., Lazio T. J. W., 2002, *arXiv e-prints*, pp astro-ph/0207156
 Cordes J. M., Lazio T. J. W., 2003, *arXiv e-prints*, pp astro-ph/0301598
 Cordes J. M., Wasserman I., 2016, *MNRAS*, 457, 232
 Dai Z. G., Wang J. S., Yu Y. W., 2017, *ApJL*, 838, L7
 Dong Y., et al., 2024, *ApJ*, 961, 44
 Gaensler B. M., Slane P. O., 2006, *ARA&A*, 44, 17
 Ghisellini G., Svensson R., 1991, *MNRAS*, 252, 313
 Goldreich P., Julian W. H., 1969, *ApJ*, 157, 869
 Hessels J. W. T., et al., 2019, *ApJL*, 876, L23
 Hilmarsson G. H., et al., 2021, *ApJL*, 908, L10
 Hotokezaka K., Kashiyama K., Murase K., 2017, *ApJ*, 850, 18
 James C. W., et al., 2022, *MNRAS*, 516, 4862
 Kasen D., Bildsten L., 2010, *ApJ*, 717, 245
 Kashiyama K., Murase K., 2017, *ApJL*, 839, L3
 Kashiyama K., Murase K., Bartos I., Kiuchi K., Margutti R., 2016, *ApJ*, 818, 94
 Katz J. I., 2021, *MNRAS*, 501, L76
 Katz J. I., 2022, *MNRAS*, 510, L42
 Kulkarni S. R., Ofek E. O., Neill J. D., Zheng Z., Juric M., 2014, *ApJ*, 797, 70
 Kumar P., Bošnjak Ž., 2020, *MNRAS*, 494, 2385
 Kumar P., Lu W., Bhattacharya M., 2017, *MNRAS*, 468, 2726
 Law C. J., Connor L., Aggarwal K., 2022, *ApJ*, 927, 55
 Lee K.-G., et al., 2023, *ApJL*, 954, L7
 Li D., et al., 2021, *Nature*, 598, 267
 Lorimer D. R., Bailes M., McLaughlin M. A., Narkevic D. J., Crawford F., 2007, *Science*, 318, 777
 Lu W., Beniamini P., Kumar P., 2022, *MNRAS*, 510, 1867
 Lyubarsky Y., 2014, *MNRAS*, 442, L9
 Lyutikov M., Burzawa L., Popov S. B., 2016, *MNRAS*, 462, 941
 Marcote B., et al., 2017, *ApJL*, 834, L8
 Margalit B., Metzger B. D., 2018, *ApJL*, 868, L4
 Metzger B. D., Piro A. L., 2014, *MNRAS*, 439, 3916
 Metzger B. D., Vurm I., Hascoët R., Beloborodov A. M., 2014, *MNRAS*, 437, 703
 Metzger B. D., Margalit B., Kasen D., Quataert E., 2015, *MNRAS*, 454, 3311
 Michilli D., et al., 2018, *Nature*, 553, 182
 Murase K., Kashiyama K., Kiuchi K., Bartos I., 2015, *ApJ*, 805, 82
 Murase K., Kashiyama K., Mészáros P., 2016, *MNRAS*, 461, 1498
 Murase K., Mészáros P., Fox D. B., 2017, *ApJL*, 836, L6
 Murase K., et al., 2021, *MNRAS*, 508, 44
 Nimmo K., et al., 2022, *ApJL*, 927, L3
 Niu C. H., et al., 2022, *Nature*, 606, 873
 Oostrum L. C., et al., 2020, *A&A*, 635, A61
 Perley D. A., et al., 2016, *ApJ*, 830, 13
 Piro A. L., Gaensler B. M., 2018, *ApJ*, 861, 150
 Planck Collaboration et al., 2016, *A&A*, 594, A13
 Platts E., Weltman A., Walters A., Tendulkar S. P., Gordin J. E. B., Kandhai S., 2019, *Physics Reports*, 821, 1
 Platts E., Prochaska J. X., Law C. J., 2020, *ApJL*, 895, L49

- Plavin A., Paragi Z., Marcote B., Keimpema A., Hessels J. W. T., Nimmo K., Vedantham H. K., Spitler L. G., 2022, *MNRAS*, **511**, 6033
- Prochaska J. X., Zheng Y., 2019, *MNRAS*, **485**, 648
- Quimby R. M., Yuan F., Akerlof C., Wheeler J. C., 2013, *MNRAS*, **431**, 912
- Rhodes L., Caleb M., Stappers B. W., Andersson A., Bezuidenhout M. C., Driessen L. N., Heywood I., 2023, *MNRAS*, **525**, 3626
- Ruiter A. J., Belczynski K., Fryer C., 2009, *ApJ*, **699**, 2026
- Spitler L. G., et al., 2014, *ApJ*, **790**, 101
- Tanaka S. J., Takahara F., 2010, *ApJ*, **715**, 1248
- Tanaka S. J., Takahara F., 2013, *MNRAS*, **429**, 2945
- Tauris T. M., Langer N., Moriya T. J., Podsiadlowski P., Yoon S. C., Blinnikov S. I., 2013, *ApJL*, **778**, L23
- Tendulkar S. P., et al., 2017, *ApJL*, **834**, L7
- Thornton D., et al., 2013, *Science*, **341**, 53
- Xing Y., Yu W., Yan Z., Zhang X., Zhang B., 2024, *arXiv e-prints*, p. [arXiv:2411.06996](https://arxiv.org/abs/2411.06996)
- Yang Y.-H., Dai Z.-G., 2019, *ApJ*, **885**, 149
- Yang Y.-P., Zhang B., 2017, *ApJ*, **847**, 22
- Yang Y.-P., Zhang B., Dai Z.-G., 2016, *ApJL*, **819**, L12
- Yang Y.-P., Li Q.-C., Zhang B., 2020, *ApJ*, **895**, 7
- Zhang G. Q., Yu H., He J. H., Wang F. Y., 2020, *ApJ*, **900**, 170
- Zhang X., et al., 2023, *ApJ*, **959**, 89
- Zhao Z. Y., Wang F. Y., 2021, *ApJL*, **923**, L17